



# 3D skull and face similarity measurements based on a harmonic wave kernel signature

Dan Zhang<sup>1,2</sup> · Zhongke Wu<sup>1,2</sup> · Xingce Wang<sup>1,2</sup> · Chenlei Lv<sup>1,2</sup> · Na Liu<sup>1,2</sup>

© Springer-Verlag GmbH Germany, part of Springer Nature 2020

## Abstract

Research regarding the similarity measurements of 3D craniofacial models (including 3D skull and face models) is an important research direction in fields such as archaeology, forensic science, and anthropology and represents a meaningful and challenging task. Its major challenges are the fact that 3D skulls are geometric models with multiple holes and complex topologies, there are facial expression changes on the 3D faces. Therefore, the general 3D shape similarity measurements, which are sensitive to boundaries and expression changes, make it impossible to simultaneously measure skull and face similarity. In this paper, we define a 3D signature to describe the pure intrinsic structure and distinguish the similar basic shape and complex topology of 3D skulls and faces: the harmonic wave kernel signature (HWKS). The HWKS is a point descriptor involving the Laplace–Beltrami operator, which is able to effectively extract geometrical and topological information from 3D skulls and faces. Based on the HWKS, we provide an effective pipeline for 3D skull and face similarity measurement by calculating the cosine distance between the HWKS values of 3D skulls and faces. By making comparisons with the wave kernel signature, the HWKS simultaneously describes both local and global properties of a shape. Results from a number of experiments have already shown that our framework is suitable for both measure 3D skull similarity and face similarity, and more importantly, measuring skull similarity and face similarity are two independent processes although using the same framework. By using the same measurement method for 3D skull similarity and face similarity, we observe an effective craniofacial relationship under unified metrics: The change rate of skull similarity is generally consistent with the corresponding face similarity, indicating the correlation between the shape of the 3D skull and its corresponding 3D face shape. And our experimental results show the rationality and effectiveness of this method, which refers to the previous researchers measure the similarity of the reconstructed face from the original skull to reflect the similarity of the original skull.

**Keywords** Laplace–Beltrami operator · Harmonic wave kernel signature · 3D skull similarity · 3D face similarity

✉ Xingce Wang  
wangxingce@bnu.edu.cn

Dan Zhang  
danz@mail.bnu.edu.cn

Zhongke Wu  
zwu@bnu.edu.cn

Chenlei Lv  
chenleilv@mail.bnu.edu.cn

Na Liu  
lna@mail.bnu.edu.cn

<sup>1</sup> School of Artificial Intelligence, Beijing Normal University, Beijing, China

<sup>2</sup> Engineering Research Center of Virtual Reality and Applications, Ministry of Education, Beijing Key Laboratory of Digital Preservation and Virtual Reality for Cultural Heritage, Beijing Normal University, Beijing 100875, China

## 1 Introduction

With the development of computer graphics and biological computing, a large number of studies on 3D craniofacial models have emerged (including 3D skull and face models) [1–3]. Compared to another biological characteristic (e.g., DNA, fingerprints), the 3D skull is a stable biological property and is resistant to fire, high humidity, and temperature changes; the 3D face is readily distinguished by the vision system of human beings. A skull is an intrinsic feature of its corresponding face, and studies on it can be applied to skull identification [4,5], craniofacial reconstruction [6] and virtual surgical planning [7,8]. A core technique involved in all of those studies is to measure the 3D craniofacial similarity. This technique is used to, for example, determine the similarity interval for skull identification or craniofa-

cial reconstruction evaluation. In this paper, we propose a similarity measure framework for 3D craniofacial models, including the similarity of 3D skull to skull and the similarity of 3D face to face based on a geometric method. And we measure the 3D skull and face models under a unified metric to eliminate errors caused by different metrics.

## 1.1 Related works

3D craniofacial similarity measurement includes 3D face similarity and 3D skull similarity. 3D face similarity measurements have been extensively studied for many years [9–15], including with respect to the global 3D face and based on the local 3D face geometric features. Lei et al. [10] extracted a face descriptor from a 3D face surface called angular radial signature (ARS) and measured 3D face similarity by using kernel principal component analysis (KPCA) and support vector machine (SVM). Emambakhsh et al. [11] proposed a novel five-step algorithm based on the nasal region for robust 3D face expression recognition. Hou et al. [12] formulated a metric learning method and constructed a decision function by incorporating Mahalanobis distance and bilinear similarity for face verification. Unfortunately, the 3D face similarity method is not suitable for 3D skulls, and few studies have ever been conducted on 3D skull similarity. This lack of research is partly attributed to the more demanding nature of acquiring and processing 3D skulls. Another reason lies in the more intricate topology of 3D skulls compared with that of 3D faces. Figure 1 shows the topological structure of a 3D skull.

Jin et al. [16] proposed a measurement method based on resampling and discrete Fourier transform (DFT) of contour pixels. Mendonca et al. [17] compared the accuracy of anthropometric measurements obtained by calipers versus two methods of 3D digital skull model. Pei et al. [18] investigated the unsupervised 3D skull similarity analysis by a random-forest-based metric. Some previous works measured the 3D skull similarity measurements through its corresponding reconstructed 3D face similarity measurements [19–21]. The consistency is observed between the similarity of the corresponding reconstructed face and that of the skull, yet this result relies on the craniofacial reconstruction method. Overall, the above methods cannot directly measure the similarity between 3D skulls, which leads to imprecise results.

Feature extraction of 3D skull and face models is the most important aspect in directly measuring skull similarity and face similarity. To extract the features of 3D skulls and faces, some works used statistical model methods [22–25]. Berar et al. [26] first applied statistical shape model (SSM) to craniofacial research, SSM is a shape analysis method that uses landmark points to represent shape models and uses statistical model to represent the transformation of shape models.

And Claes et al. [27] improved SSM by using principal component analysis (PCA). Duan et al. [24] proposed a skull identification method using PCA to match an unknown skull with 3D faces in database, in which the relationship of the 3D skull and face is obtained by using canonical correlation analysis (CCA). Shui et al. [25] analyzed how the selection of principal components (PCS) affected the analysis of craniofacial relationship and sexual dimorphism. Most researchers studied 3D skulls and faces with point cloud data, which do not include geometric information of 3D skull and face models. Meanwhile, after the reduction in dimensionality by PCA, the data cannot contain all the information on the skull and face models.

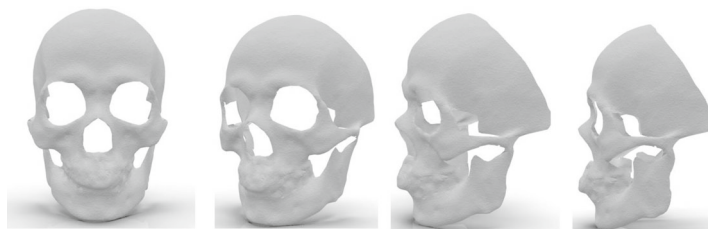
The multi-boundary 3D skull and the 3D facial expressions are relatively difficult to process, especially in terms of the similarity problem. In recent years, research has suggested that expression variation can be modeled as isometric or approximate isometric transformations [28–30]. Therefore, we consider extracting intrinsic characteristics of 3D skull and face models based on the spectral shape descriptors. Spectral shape descriptors are derived from the eigenvalues  $\lambda_i$  and eigenfunctions  $\phi_i$  of the Laplace–Beltrami operator (LBO) to compute local shape descriptors [31].

The global point signature (GPS) is a global spectral shape descriptor, which maps 3D shapes into an infinite-dimensional space called global point signature embedding dominant [32,33]. Assume a heat source  $\mu_{0(x)}$  on a manifold; the heat kernel signature (HKS) was proposed by Sun et al. [34]:  $HK S_t(x, y)$  defines the heat transferred from point  $x$  to point  $y$  at time  $t$ .  $HK S_t(x, x)$  is the amount of heat retained at point  $x$  after time  $t$ . However, the above spectral shape descriptors use low-pass filters, which may filter out the high-frequency information of shapes. The wave kernel signature (WKS) [35] was proposed by using a band-pass filter to clearly separate different sets of frequencies of shapes and the WKS allows access to high-frequency information and is independent of time parameters compared to the HKS.

## 1.2 Contribution

The problem of simultaneously measuring 3D skull similarity and face similarity by a single method remains difficult. In this paper, we propose an advanced method for exploiting intrinsic information of shapes to measure 3D skull similarity and face similarity under a unified standard of measurement. In this paper, we define a novel descriptor that inherits the advantages of the WKS and can distinguish the different shape models from the same shape class. Our method pays more attention to the description of shape details, so it can better reflect the differences of different shapes in the same

**Fig. 1** Different views on the topological structure of a 3D skull (to be more specific, unlike 3D human face models with a single outer boundary, 3D skulls contain orifices with varied sizes in the regions of eyes, nose, ears, and cheeks, thus rendering the models as multiboundary surfaces.)



class of shape than other methods. The contributions of our study are as follows:

- We propose a novel shape descriptor HWKS, which effectively balances the multi-scale characteristics of the WKS and describes the local and global properties of 3D skull and face at the same time. The HWKS can not only distinguish the similar basic shapes and complex topological structures of 3D skull models but also is robust to approximate isometric transformation of 3D facial expression;
- We propose a pipeline that can directly and efficiently measure 3D skull similarity and face similarity which is not affected by 3D coordinates. This pipeline does not require to pre-fill holes in the skull models, and it is robust to facial expression changes, and the needs of researchers to calculate arbitrary craniofacial similarity are satisfied by the same measurement method;
- We validate the effectiveness of our proposed method with two different experimental strategies based on the Asian Mongolian craniofacial database. More importantly, our experimental results show the validity and rationality of the fact that 3D skull similarity can be presented by its corresponding or reconstructed face similarity, which has not been studied in details in previous works [19–21] but is significant.

The remaining parts of the paper are organized as follows. In Sect. 2, we illustrate the fundamentals and pipeline of our proposed method. In Sect. 3, we provide the harmonic wave kernel signature in detail and construct a similarity measurement for 3D skulls and faces. In Sect. 4, we demonstrate our methods on the Asian Mongolian craniofacial database for experiments and analyze the craniofacial relationship. Finally, we draw conclusions regarding our study in Sect. 5.

## 2 Fundamentals and pipeline

In this section, we remain within the Riemannian geometric framework and introduce the pipeline of 3D skull similarity measurement and 3D face similarity measurement. Our method is based on the Laplace–Beltrami operator (LBO) and

the eigenfunction and eigenvalue of the LBO can be defined as different spectral shape descriptors. By calculating the distances between spectral shape descriptors defined on shapes, we obtain 3D skull similarity and 3D face similarity. In this section, the definition and the discrete calculation of the LBO are first given; then the ZoomOut shape correspondence [36] is introduced for finding the efficient correspondence points of a pair of shapes; the general framework for 3D skull similarity measurement and 3D face similarity measurement is ultimately shown.

### 2.1 Laplace–Beltrami operator

Consider a shape as a two-dimensional smooth compact manifold  $M$  equipped with a Riemannian metric  $g$ , possibly with a boundary. On the surface of manifold  $M$ , we define a novel shape descriptor, which is in turn closely connected with the notion of the LBO. Let  $f$  be a  $C^2$  real-valued function, defined on manifold  $M$ . The LBO is a differential operator defined by the divergence of the gradient of  $f$  as follows:

$$\Delta f = \nabla \cdot \nabla f = \nabla^2 f = \frac{\partial^2 f}{\partial x^2} + \frac{\partial^2 f}{\partial y^2} + \frac{\partial^2 f}{\partial z^2} \quad (1)$$

Explicitly, the LBO of a function  $f$  in local coordinates obtained by equipping with a Riemannian metric  $d$  can be expressed as follows [37]:

$$\Delta f = \nabla \cdot \nabla f = \frac{1}{\sqrt{G}} \sum_{i,j=1}^n g^{ij} \frac{\partial}{\partial x^i} \left( \sqrt{G} g^{ij} \frac{\partial f}{\partial x^j} \right) \quad (2)$$

In the above equation,  $g$  is a metric tensor defined on the surface of Riemannian manifold  $M$ ,  $g^{ij}$  is the inverse metric tensor, and  $G$  is the determinant of the matrix  $g^{ij}$ . Since the LBO is self-adjoint and semipositive definite, the LBO on  $M$  is decomposed into the matrix product of the eigenvalue and eigenfunction:

$$\Delta_M \phi_i = \lambda_i \phi_i \quad (3)$$

where  $\phi_i$  is the  $i$ th eigenfunction, corresponding to the eigenvalue  $\lambda_i$ . When  $M$  is a connected manifold without boundary, the first eigenvalue is 0, with the corresponding constant

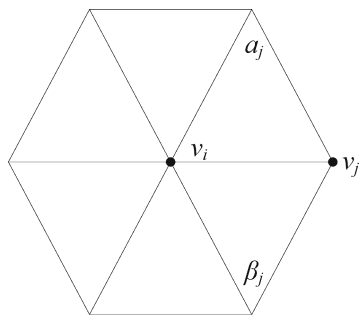


**Fig. 2** The triangular surface sketch of a vertex  $v_i$

eigenfunction, and the smallest nonzero eigenvalue is  $\lambda_1$ . We can order the eigenvalues as:  $0 = \lambda_0 < \lambda_1 \leq \lambda_2 \leq \lambda_3 \leq \dots$ , where the set of corresponding eigenfunctions is:  $\phi_1, \phi_2, \phi_3, \dots$ , and each vertex has a different eigenfunction. In this paper, we consider shapes represented as triangle meshes in the discrete setting. The discrete LBO at the vertex  $v_i$  of the triangle mesh can be defined as follows:

$$\Delta f(v_i) = \frac{1}{2} \sum_{v_j \in \text{Nei}(v_i)} (\cot \alpha_{ij} + \cot \beta_{ij}) |f(v_j) - f(v_i)| \quad (4)$$

where  $v_i$  is the  $i$ th vertex on the triangle mesh model,  $\text{Nei}(v_i)$  is the adjacent vertex set of  $v_i$ ,  $\alpha_{ij}$  and  $\beta_{ij}$  are angles on two sides of the edge connecting  $v_i$  and  $v_j$ , as shown in Fig. 2.

## 2.2 Functional maps and ZoomOut

It is necessary to find a point-to-point correspondence of a pair of shapes in advance before measuring the similarity. Recently, functional maps [38] have exhibited performance in finding the corresponding points between a pair of 3D shapes. The main idea of functional maps is to identify correspondences between a pair of manifolds  $M$  and  $N$  by a point-wise map:  $T : L^2(M) \rightarrow L^2(N)$ ,  $L^2$  is Hilbert space composed of inner product of finite points. The map  $T$  induces a linear functional correspondence:  $T_F(f) = g$  and  $g = f \circ T^{-1}$  where  $f : M \rightarrow R$  and  $g : N \rightarrow R$ . Suppose that  $f : M \rightarrow R$  can be represented as a linear combination of basis functions  $f = \sum_i a_i \phi_i^M$  in the function space of  $M$  equipped with a basis. Then,  $T_F(f)$  is defined as follows:

$$T_F(f) = T_F \left( \sum_i a_i \phi_i^M \right) = \sum_i a_i T_F \left( \phi_i^M \right) \quad (5)$$

In addition, if suppose that  $g : N \rightarrow R$  can be represented as a linear combination of basis functions  $g = \sum_i b_i \phi_i^N$  in the function space of  $N$  and  $c_{ij}$  is a possibly infinite matrix

of real coefficients, Eq. 5 is expressed as follows:

$$T_F(f) = \sum_j \sum_i a_i c_{ij} \phi_j^N \quad (6)$$

where  $c_{ij}$  is independent of  $f$  and is completely determined by the bases and map  $T$ . Ovsjanikov et al. [38] used the first  $n$  eigenfunctions of LBO as the bases for their functional representations ( $n=100$ , independent of the number of points on the shape). For a fixed choice of basis function  $\phi^M$ ,  $\phi^N$ ,  $c_{ij}$  is a matrix of real coefficient.

Therefore, let  $f$  be represented as a vector of coefficients  $\mathbf{a} = (a_0, a_1, \dots, a_i, \dots)$  and  $g$  is represented as a vector of coefficients  $\mathbf{b} = (b_0, b_1, \dots, b_i, \dots)$ , where a functional map  $T_F$  is a matrix  $C$ :  $\mathbf{b} = C\mathbf{a}$ . The optimal solution  $C$  is obtained by solving linear equations constructed by function preservation contradictions, including descriptor preservation, landmark correspondence and segment correspondence. Descriptor preservation describes the geometry characteristics of any point on the shape (such as HKS, WKS); landmark correspondence is to encode the distance function of the landmark points or the normal distribution function around the landmark points as a functional constraint; segment correspondence is to establish the correspondence of the indicator functions on the segments of all segments of a pair of shapes as functional constraints [38]. After obtaining the  $C$ , the point-wise correspondence between a pair of shapes was found [38] by multiple iterations using the least squares algorithm.

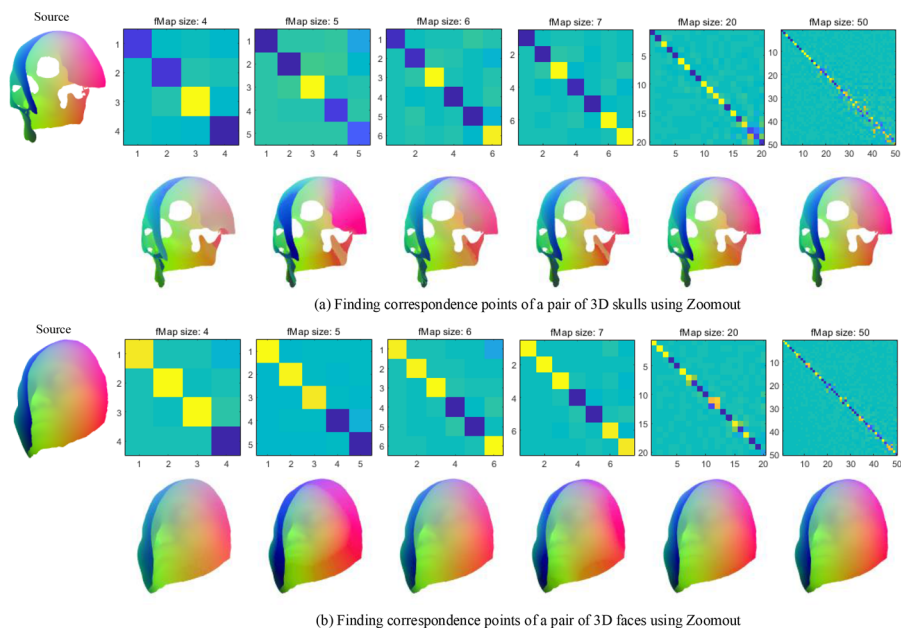
Based on the method of functional maps, Simone Melzi et al. proposed a very simple and efficient map refinement method called “ZoomOut” for rapidly determining shape correspondences by iterative up-sampling in the spectral domain [36]. When given an input  $k_M * k_N$  functional map  $C_0$ , they extend it to a new map  $C_1$  of  $(k_M + 1) * (k_N + 1)$  without other information, and then they iterate this procedure to obtain progressively larger functional maps  $C_0, C_1, C_2, \dots, C_n$  until some sufficiently large  $n$ . The key parameter for the initialization is the size of the functional maps, which is set as  $k_M = k_N = 4$  in most settings.

In our paper, we obtain the initial corresponding point set (CPS) between a pair of 3D shapes using the ZoomOut, as shown in Fig. 3. Then, we can measure the 3D skull similarity and face similarity by calculating the distance between descriptors defined on the shapes CPS.

## 2.3 Pipeline

In this paper, we propose a general pipeline for 3D skull similarity and 3D face similarity measurements. Figure 4 schematically describes the generic framework for 3D skull similarity and 3D face similarity measurement based on the HKWS. *Importantly, both skull similarity measurement and*

**Fig. 3** Finding the correspondence point set of a pair of 3D skulls (a) and a pair of 3D faces (b) using ZoomOut, the color coding represents the correspondence points



face similarity measurement can be implemented separately according to task requirements, not necessarily simultaneously.

The specific five steps of the pipeline are as follows:

- A. *Input 3D models* The first step is to input a pair of 3D skulls or faces. This paper deals with triangle mesh models including the effective geometric information and topology;
- B. *Calculate the LBO* Given a pair of 3D skulls or faces, a real-valued function  $f$  is defined. We calculate the eigenvalues  $\lambda_i$  and eigenfunctions  $\phi_i$  of the LBO of 3D skulls or shapes;
- C. *Obtain the CPS* Based on the eigenvalues  $\lambda_i$  and eigenfunctions  $\phi_i$ , we use the ZoomOut to obtain the CPS of a pair of 3D skulls or faces;
- D. *Calculate the HWKS* We calculate the HWKS of 3D skulls or faces by choosing two efficient energy levels and select the HWKS values of the skulls CPS or faces CPS;
- E. *Output similarity results* Based on the HWKS values of CPS, we define a similarity measurement by using the cosine distance which satisfies non-negativity, nullity and symmetry.

### 3 Harmonic wave kernel signature and 3D skull similarity measurement

In this section, we propose a method to construct the HWKS that provides an optimal trade-off between discernment and invariance and analyze the invariance of the HWKS. Last,

we define a general measurement for calculating 3D skull similarity and 3D face similarity using the cosine distance.

#### 3.1 The wave kernel signature

The WKS is introduced by Aubry et al. [35], which can be naturally interpreted in the framework of quantum mechanics as the average probability of finding a particle with a given energy distribution  $f_E$  at a specific point  $x \in M$ :

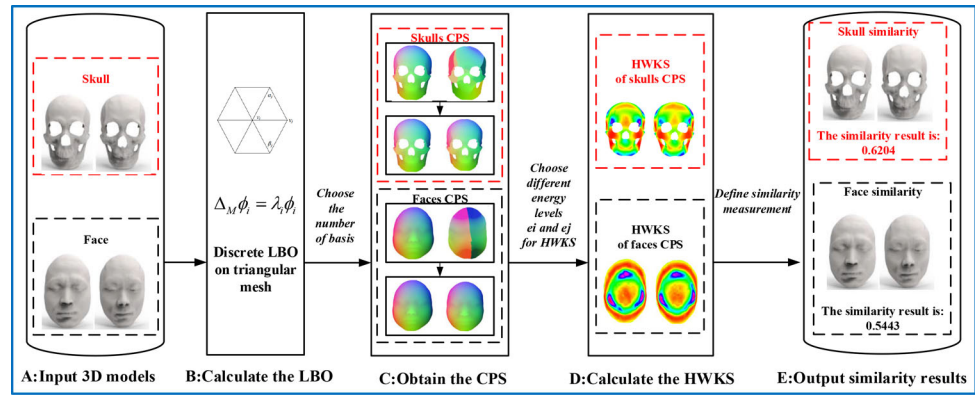
$$\frac{\partial \phi}{\partial t}(x, t) = i \Delta \phi(x, t) \tag{7}$$

$\phi(x, t)$  is the wave function which expresses the energy oscillation, where  $\Delta$  is the LBO and  $i$  is imaginary unit; the product of the LBO and  $i$  ensures that the energy will not decay after oscillating at different frequencies. When  $t$  is 0, the expectation of  $\phi(x, t)$  is the approximate energy  $E$ . The author choose the eigenvalues  $\lambda_k$  of the LBO defined on the surface of the shape as the distribution parameter of energy distribution  $f_E$ , while the energy is directly related to the eigenvalues  $\lambda_k$  of the LBO [35]. When  $t = 0$ , the  $f_E(\lambda_k)$  denotes the energy distribution of the particle with parameter  $\lambda_k$ , and the wave function  $\phi(x, t)$  of the particle is given by the following:

$$\phi(x, t) = \sum_{k=0}^{\infty} e^{i\lambda_k t} \phi_k(x) f_E(\lambda_k) \tag{8}$$

The probability of measuring the particles at point  $x$  is  $|\phi(x, t)|^2$ . Since the probability distribution is time-independent, the WKS is defined as the average probability

**Fig. 4** The pipeline of 3D skull similarity measurement and 3D face similarity measurement



of measuring a particle in  $x$ :

$$WKS(x, E) = \lim_{T \rightarrow \infty} \frac{1}{T} \int_0^T |\phi(x, t)|^2 \tag{9}$$

The functions of  $e^{i\lambda_k t}$  are orthogonal for the  $L^2$  norm:

$$WKS(x, E) = \sum_{k=0}^{\infty} \phi_k^2(x) f_E(\lambda_k) \tag{10}$$

Because the energy probability distribution  $f_E^2$  follows a log-normal distribution with parameter  $\sigma$ , the author of the WKS defined the WKS at a point  $x \in M$  as a real valued function in the logarithmic energy scale  $e_N = \log(E)$  [35]. When  $\cdot$  represents the dot product and  $WKS(x, \cdot)$  describes the binary operation of point  $x$  on  $R$ , the wave function  $WKS(x, e_N)$  of the particle at a point  $x \in M$  is given by the following:

$$\begin{cases} WKS(x, \cdot) : R \rightarrow R; \\ WKS(x, e_N) = C_e \sum_k \phi_k^2(x) e^{\frac{-(e_N - \log \lambda_k)^2}{2\sigma^2}} \end{cases} \tag{11}$$

where  $C_e = (\sum_k e^{\frac{-(e_N - \log \lambda_k)^2}{2\sigma^2}})^{-1}$  is the regularized WKS function. In this function, the time parameter has been replaced by the energy, which is directly related to the eigenvalues of the LBO.

### 3.2 Harmonic wave kernel signature

In [35], the author computed the first  $M = 300$  eigenvalues of the LBO and evaluated the WKS at  $N = 100$  values  $e_N$  which make up different energy levels to describe the global or local shape features; they used  $e_{\min} = \log(\lambda_1) + 2\sigma$ , the logarithm of the smallest nonzero eigenvalue and  $e_{\max} = \log(\lambda_M) - 2\sigma$ . With the linear increment  $q = (e_{\max} - e_{\min})/N$  and the

variance was set to  $\sigma = 7q$ , we can obtain the following:

$$\begin{aligned} e_{\min} &= \frac{N+2q}{N+4q} \log(\lambda_1) + \frac{2q}{N+4q} \log(\lambda_M) \\ e_{\max} &= \frac{2q}{N+4q} \log(\lambda_1) + \frac{N+2q}{N+4q} \log(\lambda_M) \\ \text{diff} &= \frac{N}{(N-1)(N+4q)} (\log(\lambda_M) - \log(\lambda_1)) \\ e_n &= e_{\min} + (n - 1) * \text{diff} \end{aligned} \tag{12}$$

The WKS is a stable and highly informative descriptor, it has multi-scale characteristics by selecting different energy levels.

$$\begin{bmatrix} WKS(x_1, e_1), WKS(x_1, e_2), \dots, WKS(x_1, e_N) \\ WKS(x_2, e_1), WKS(x_2, e_2), \dots, WKS(x_2, e_N) \\ \dots \dots \dots \\ WKS(x_n, e_1), WKS(x_n, e_2), \dots, WKS(x_n, e_N) \end{bmatrix} \tag{13}$$

Equation (13) shows the WKS matrix of  $M$  at  $N$  energy levels, where  $n$  is the number of points on  $M$  and  $WKS(x_n, e_N)$  represents the WKS of the vertices  $x_n$  at the energy level  $e_N$ , and each column represents the WKS of each point at different energy levels.

Figure 5 shows the WKS values at different energy levels of a 3D skull and a 3D face. We hope to obtain the largest possible amount of information about skulls and faces for the similarity calculation. In this paper, we want to construct a shape descriptor that can reflect the global and local features of shapes at the same time. Based on the synthetic feature method in machine learning, we propose a novel shape descriptor called the harmonic wave kernel signature, which is significantly more discriminative than the WKS, which functions by simultaneously simulating the processes of high-energy and low-energy particle oscillation on the shape surface:

$$\begin{cases} HWKS(x, \cdot) : R \rightarrow R; \\ HWKS(x, e_H, e_L) = H_e \frac{WKS(x, e_H)}{WKS(x, e_L)} \\ H_e = \sum_k e^{\frac{(e_H - e_L)(2 \log \lambda_k - e_H - e_L)}{2\sigma^2}} \end{cases} \tag{14}$$

**Fig. 5** The WKS values at different energy levels of a 3D skull and a 3D face (for WKS, if the quantum particle with higher energy level is selected, then the shorter the wavelength is, the closer it is to the point on a shape. In this case, the local characteristics of the skull or face are reflected. Conversely, the quantum particle with lower energy level reflects the global characteristics of the skull or face.)

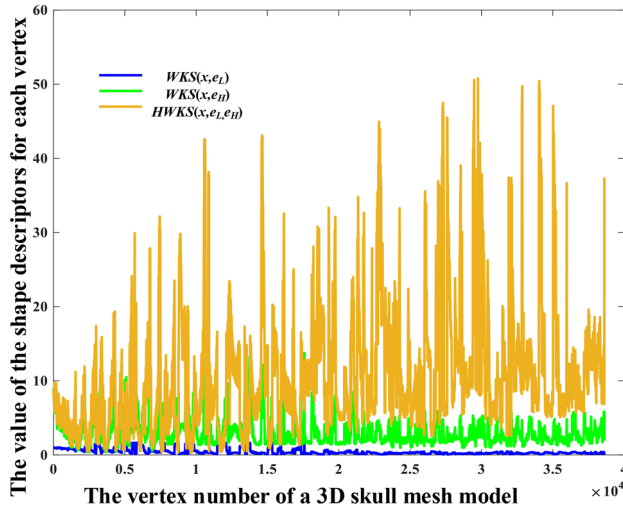
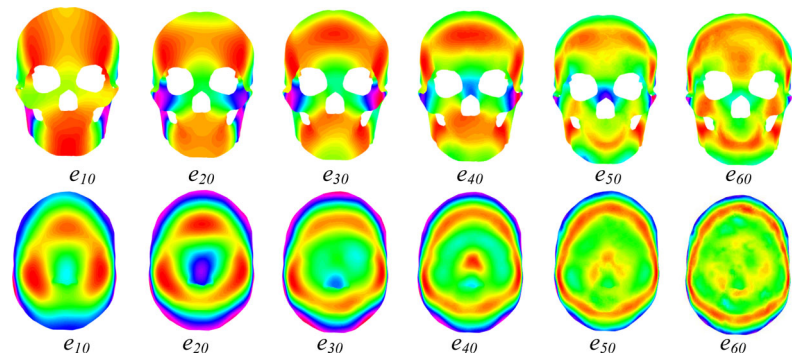


**Fig. 6** Schematic diagram of HWKS values for each vertex (HWKS expands the difference between different points and accurately describes the details of the 3D skull model)

where  $e_L$  and  $e_H$  denote low energy and high energy levels, respectively.  $H_e$  is the regularized HWKS. We purposefully introduce two different energy levels to balance the global and local characteristics of shapes, the schematic diagram of HWKS as shown in Fig. 6 for each vertex.

Combining Eqs. (12) and (14), we can obtain the following:

$$\begin{aligned}
 e_H - e_L &= (e_{min} + (H - 1) * diff) \\
 &- (e_{min} + (L - 1) * diff) \\
 &= (H - L) * diff
 \end{aligned}
 \tag{15}$$

where  $diff$  is a constant. To show the highly discriminating feature of 3D skull and face model, we choose the higher energy  $H$ , in which case the increase in the value of  $(H - L)$  coincides with the improvement of the result. It is noteworthy that the value of  $L$  cannot be too small if the global property of the shape is to be maintained. Empirical values are given as  $L$  and  $H$  in the experiment.

### 3.3 Invariance of the harmonic wave kernel signature

The HWKS inherits the advantages of WKS, rendering it invariant under different transformations. This invariance is as follows:

*HWKS is intrinsic* If we separately calculate the HWKS before and after the isometric shape change, the theoretical value of the HWKS remains unchanged: that is,  $T : X \rightarrow Y$  is an isometric deformation,  $HWKS(T(x), e_H, e_L) = HWKS(x, e_H, e_L)$  for all  $x \in M$ ;

*HWKS has topological robustness* In many real scenarios, the shape undergoes not only isometric deformation but also exhibits “topological noise”. The WKS uses a bandpass filter for higher stability, and it is thus characterized by the high robustness to topological changes. Inheriting this characteristic, the HWKS is also robust to topological changes.

*HWKS is discriminative* Indeed, the HWKS is a point signature over the energy levels of particles that are directly related to different scales, for which the higher energies correspond to local geometry whereas smaller energies correspond to properties induced by the global geometry.

### 3.4 Craniofacial similarity measurement

Because the shapes of different craniofacial models are very similar, in order to compare the similarities of the same types of shapes, we normalize the HWKS of craniofacial models. Normalizing the HWKS can not only improve the calculation accuracy but also ensure the reliability of the similarity calculation. In our study, we use Z-score normalization, where  $\mu_{HWKS}$  is the mean HWKS of the craniofacial models and  $\sigma_{HWKS}$  is the standard deviation of the HWKS of craniofacial models,  $HWKS^*_M$  denotes the  $HWKS_M$  of craniofacial model  $M$  after normalization.

$$HWKS^*_M = \frac{HWKS_M - \mu_{HWKS}}{\sigma_{HWKS}}
 \tag{16}$$

After normalizing the HWKS, we can define the similarity measurement between a pair of skulls or a pair of faces.

The cosine distance can effectively avoid the differences of individual degrees, devote more attention to the difference between the dimensions, and can converge the range of distance to  $[0, 2]$ , which can effectively measure the difference between shapes. In this paper, cosine distance is selected to construct the similarity calculation index, which measures the difference between two individuals by calculating the cosine distance of the angle between two vectors. The closer the cosine distance is to 0, the closer the direction of the two vectors is; when the cosine distance is closer to 2, it is indicated that the two vectors have opposite directions. In other words, the closer the cosine distance is to 0, the more similar the two shapes are, and vice versa. When the cosine distance is 0, the two shapes are the same. Based on the CPS results of a pair of shapes  $P$  and  $Q$  obtained by using the ZoomOut which is introduced in Sect. 2.2, we directly calculate the cosine distance between a pair of shapes CPS as follows.

$$d(P, Q) = 1 - \frac{\sum_{i=1}^n \text{HWKS}^*(x_{pi})\text{HWKS}^*(x_{qi})}{\sqrt{\sum_{i=1}^n \text{HWKS}^*(x_{pi})^2} \sqrt{\sum_{i=1}^n \text{HWKS}^*(x_{qi})^2}} \quad (17)$$

where  $\text{HWKS}^*(x_{pi})$  and  $\text{HWKS}^*(x_{qi})$  represent the corresponding point  $i$  on shapes  $P$  and  $Q$ , and  $n$  is the number of points of the  $P$  and  $Q$  CPS. The  $d(P, Q)$  distance satisfies the following properties:

- *Non-negativity*  $d(P, Q) \geq 0$
- *Nullity*  $d(P, Q) = 0$  if and only if  $P = Q$
- *Symmetry*  $d(P, Q) = d(Q, P)$

And to fit the concept of craniofacial similarity (i.e., the more similar the two craniofacial models are, the larger the similarity measure is), we define the  $D_{\text{cosine}}(P, Q)$  denoting  $1/(1+d(P, Q))$  to represent the craniofacial similarity measurement range from  $[1/3, 1]$ . The larger the  $D_{\text{cosine}}(P, Q)$  values are, the more similar the shape  $P$  and  $Q$  are. When  $P = Q$ ,  $D_{\text{cosine}}(P, Q) = 1$ , meaning that  $P$  and  $Q$  are the same craniofacial model. More importantly, when the two craniofacial models are the most dissimilar,  $D_{\text{cosine}}(P, Q) = 1/3$ , rather than 0, as a special 3D model, craniofacial model has certain similarity in shape, so we define the minimum value of craniofacial similarity as  $1/3$  to conform to human subjective judgment.

$$D_{\text{cosine}}(P, Q) = \frac{1}{1 + d(P, Q)} \quad (18)$$

## 4 Experimental results

In this section, we demonstrate the experimental results obtained based on a craniofacial database. We do experiments on MATLAB 2015 on 64 bit 32G memory, win10 system. The time complexity of calculating craniofacial similarity is  $O(n^2)$ , and  $n$  is the number of sampling points on the 3D craniofacial model. The experiments include five parts: first, we provide the introduction to the craniofacial database; second, we show the effectiveness of the HWKS compared to GPS, HKS and WKS; third, we conduct the skull similarity and face similarity measurement on morph data generated by linear interpolation; fourth, we conduct the skull similarity and face similarity measurement on real data randomly selected from the craniofacial database; finally, we analyze the craniofacial relationship and offer the discussion of above experiments.

### 4.1 Database

The Asian Mongolian craniofacial database, on which our experiments are based, consists of data from 140 volunteers at Xianyang Hospital, which is located in northwestern China. The majority of the 140 volunteers, aged from 19 to 75, belong to the Han ethnic group living in northern China. The data were collected in the form of CT head scans, by a clinical multi-slice CT scan system (Siemens Sensation16). During the data collection process, the volunteers were supine, with their hands naturally sagging, their feet close together, and their head was not tilted. Axial position helical scanning was used to reconstruct a thickness of 0.75mm. The data collected for all samples were stored in the form of standard DICOM 3.0 images with an inter-layer slice resolution of  $512 \times 512$ . Since the 3D face and skull models used for similarity measurements usually must be complete, the craniofacial models of the data have been preprocessed. Some of the processes that they undergone through include model restoration, unified coordinate system, data standardization, model clipping, and the elimination of translation and rotation effects. It is also worth noting that the impacts of data size and posture have been eliminated by the sufficiently large data scale and the unified coordinate system shared by the models. Figure 7 shows examples from the craniofacial database.

### 4.2 Effectiveness of the HWKS

After many experiments, we obtain the empirical values of the energy parameters for the HWKS. Compared with 3D face models, the more visually noticeable characteristics of 3D skull models result in relative prominence among data: the thresholds for faces to be properly described are the energy level  $H = 80$ ,  $L = 30$ , while those values for skulls are  $H = 60$ ,  $L = 10$  (for the discussion of the energy param-



**Fig. 7** Examples of male and female skulls and faces in the craniofacial database

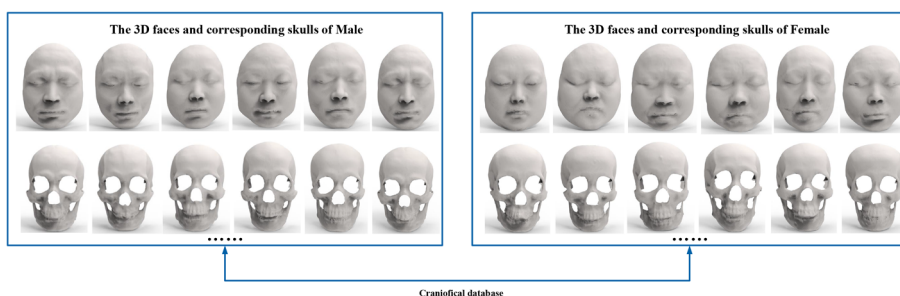
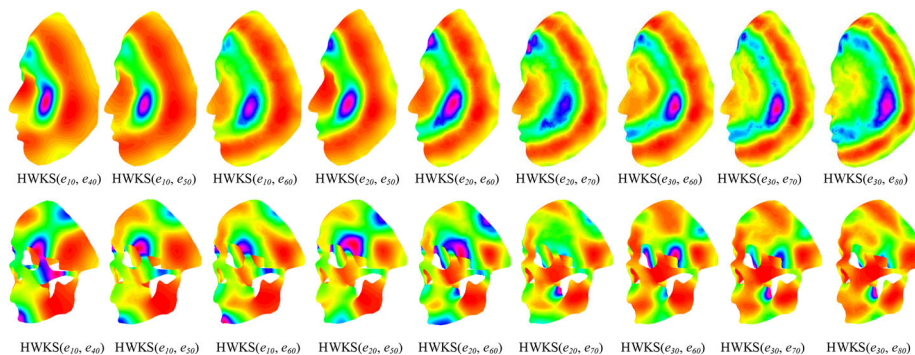


**Fig. 8** Choosing the values of the energy parameters for HWKS



eter selection for different genders, please refer to [39]). The HWKS can simultaneously describe the local and global properties of the skull and face models, which can be seen from Fig. 8.

The HWKS can simultaneously represent the local and global features of 3D skull and face models by introducing two energy parameters: high energy and low energy. As its result, the HWKS expands the difference between different points as shown in Fig. 6 and accurately describes the details of the 3D skull and face models and it leads to the different regions on the surface of 3D craniofacial model can be clearly separated in Fig. 9. Figure 9 shows the 3D skull and face describing results generated by using HKS, GPS, WKS, and HWKS. From Fig. 9, we found that HWKS can separate more color spots (the same color spot or region represents the point with similar shape surface value) on the surface of 3D skull and face model, which means that different regions of 3D skull and face model are displayed. The HWKS offers superior abilities for feature localization and distinguish different regions in the model. This difference in model descriptions corroborates the suitability of the HWKS in describing 3D skulls and faces.

### 4.3 Experiments on morph data

Usually, people cannot intuitively identify skull similarity, except for experts studying archaeology and forensic science, who are able to delineate the intricate differences between different skulls. Through objective deformation operations, we obtain the actual ground-truth value of similarity measurement, with which we will compare our experimental

results to evaluate the effectiveness of our 3D skull similarity and face similarity measurement algorithm. We calculate the similarity between the skull models and morph skull models through linear interpolations, and the same operation is performed on the face.

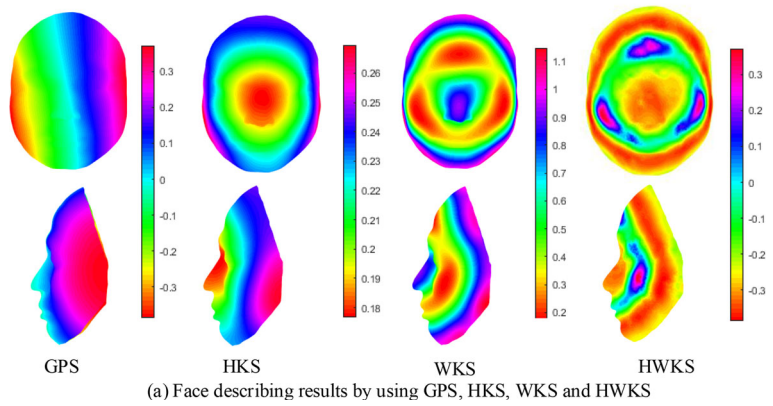
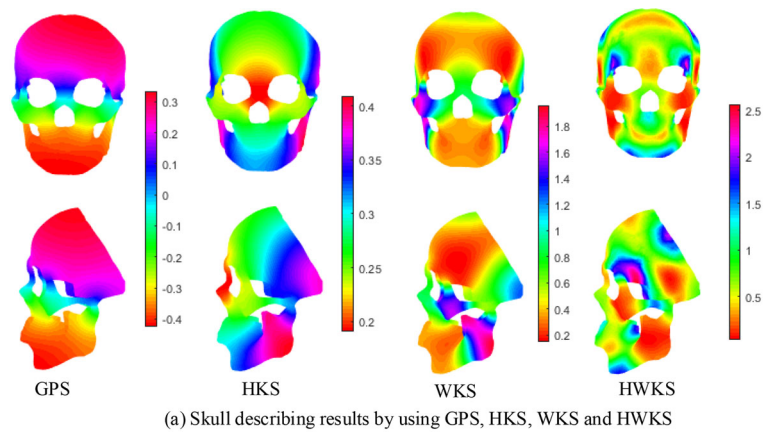
Two 3D craniofacial models,  $S_1$  and  $S_2$ , are randomly selected from the craniofacial database. Based on the linear interpolation deformation process between the two models, the four models in the middle are selected out of all of the  $S_2$  models generated from the  $S_1$  deformation. We deform the  $S_1$  and  $S_2$  (for both male and female), simulating the four morph models generated from  $S_1$  and  $S_2$ , which are defined as  $M_1, M_2, M_3$ , and  $M_4$ :  $M_i = (1 - i\alpha) * S_1 + i\alpha * S_2$ . The 3D craniofacial models of male and female generated from the  $S_1$  and  $S_2$  deformation processes are shown in Figs. 10 and 11, respectively.

Linear interpolation deforms the coordinates of the spatial points of the morph model. Therefore, we also use the Euclidean distance between the coordinates of the spatial points to define the similarity theoretical value. The calculation formula is:

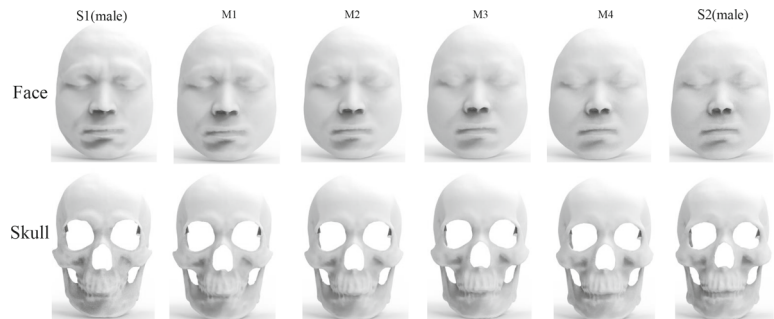
$$\text{similarity}(a, b) = \frac{1}{(1 + \sqrt{\sum_{i=0}^{\text{num}} ((x_{ai} - x_{bi})^2 + (y_{ai} - y_{bi})^2 + (z_{ai} - z_{bi})^2))}} \tag{19}$$

$a$  and  $b$  are selected from  $S_1, S_2, M_1, M_2, M_3$  and  $M_4$ , num is the number of corresponding points set (CPS) of the model, calculated by ZoomOut, the similarity theoretical values are

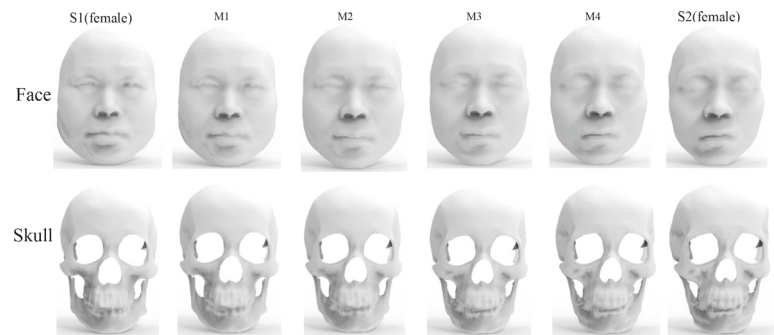
**Fig. 9** 3D skull and face models describing results by using HKS, GPS, WKS and HWKS (we map the feature values of each point of 3D skull and face with different color bar, the same color spot or regions represents the point with similar shape surface value)



**Fig. 10** Deformation faces and skulls of male generated from male S1 and S2



**Fig. 11** Deformation faces and skulls of female generated from female S1 and S2



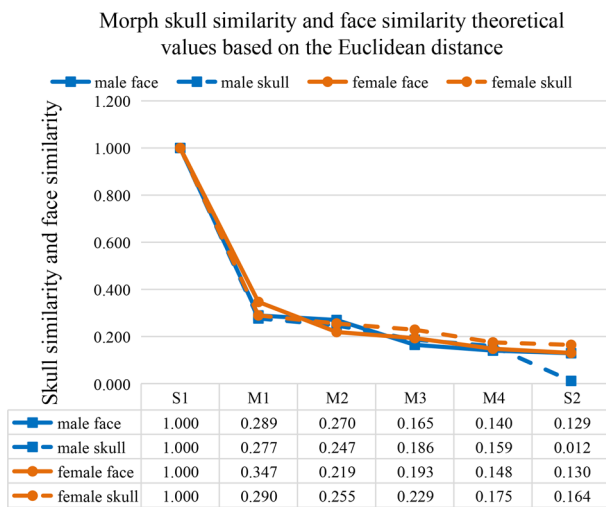


Fig. 12 Morph skull similarity and face similarity theoretical values based on Euclidean distance

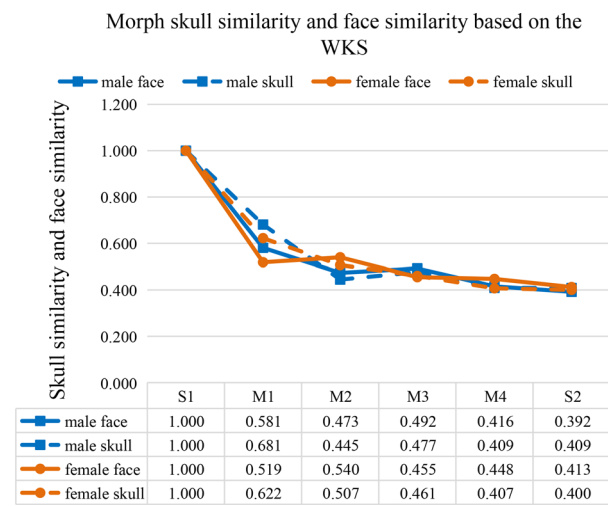


Fig. 14 Skull similarity results for males and females using WKS

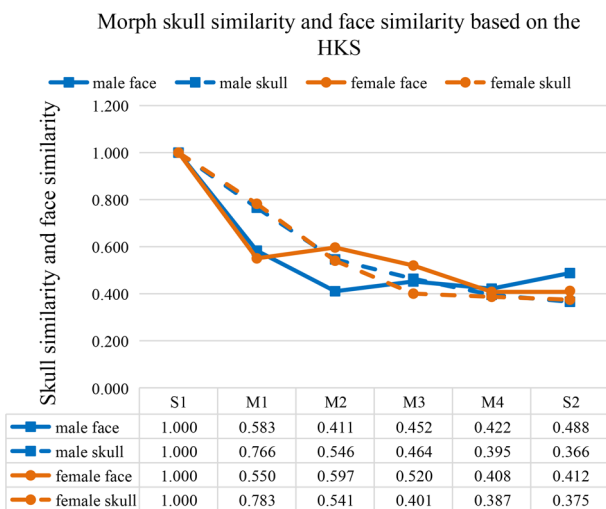


Fig. 13 Skull similarity results for males and females using HKS

shown in Fig. 12 and the trend of the similarity theoretical value decreases.

After the deformation process, we calculate the 3D skull similarity and face similarity with three different methods, namely HKS and cosine distance, WKS and cosine distance, and HWKS and cosine distance, whose results are respectively shown in Figs. 13, 14, and 15. Theoretically, the similarity between S1 and S2 should exhibit a decreasing trend.

From Fig. 13, when the HKS is used to describe the 3D skull and face, the results show that the similarity results are not consistent with the similarity theoretical values, and the face similarity does not completely decline. The explanation for such results is that because of the low-pass filter it applies, the HKS is unable to describe the subtleties between distinctive skull models.

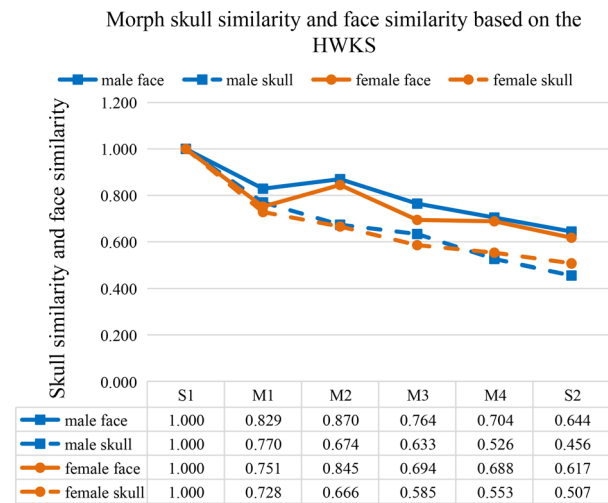














Fig. 15 Skull similarity results for males and females using HWKS













From Fig. 14, when the WKS is applied to describe the skull and face, the bandpass filter it uses determines that it is more capable of presenting the differences between skulls and the differences between faces. The results show that the trend of similarity results are basically consistent with the trend of similarity theoretical values. However, since the WKS can only select one energy parameter for each calculation, it is almost unlikely to describe both the global and local properties of the skulls and faces at the same time. Therefore, skulls and faces cannot be well classified when the WKS is used as the descriptor to calculate similarity.

From Fig. 15, when using the HWKS, the trends of face similarity and skull similarity are essentially consistent with the trend of the similarity theoretical values of males and females. Simultaneously, the skulls and faces can be clearly and effectively classified based on the similarity results. The above results illustrate that the HWKS proposed in this paper

**Fig. 16** Skull similarity and face similarity results of males

Number	001-2354	001-3921	004-5343	007-4952	002-3852	003-4302
Face						
Skull						
Face Similarity results	1.0	0.5443	0.5278	0.4845	0.4631	0.4167
Skull Similarity results	1.0	0.5690	0.5201	0.5046	0.4892	0.4414

**Fig. 17** Skull similarity and face similarity results of females

Number	002-1642	009-3547	009-4816	009-5803	006-4142	011-4517
Face						
Skull						
Face Similarity results	1.0	0.5971	0.5177	0.5028	0.4890	0.4316
Skull Similarity results	1.0	0.6204	0.5785	0.5171	0.4874	0.4215

demonstrates its effectiveness in representing the local and global properties of the skulls, as well as its ability to contribute to much more accurate results. In this paper, the HWKS is used to calculate cosine distance, which is a non Euclidean feature, while the theoretical value is calculated by the 3D point coordinates of the craniofacial models, which is an Euclidean feature. Therefore, the similarity calculated by the method proposed in this paper is consistent with the trend of theoretical value of similarity, which can verify the effectiveness of this method.

Although the results of Figs. 14 and 15 show that the similarity results of WKS and HWKS are basically consistent with the trend of similarity theoretical value, it is obvious that the similarity curve of skull model and facial model in Fig. 15 can be separated compared to Fig. 14. Because the WKS only can select one energy parameter for each calculation, it is almost unlikely to describe both the global and local

properties of the skulls and faces at the same time. In contrast, skulls and faces can be well classified when the HWKS is used as the descriptor to calculate similarity. All of the above findings from our experiment demonstrate the limitations of using the HKS or the WKS in describing 3D skull model similarities. The unexpected turning points are shown in the results where the HKS and WKS are used to calculate skull similarity and face similarity for both males and females.

#### 4.4 Experiments on real data

To further verify that the skull similarity measurement proposed in this paper is effective, we use the face similarity results to evaluate the skull similarity results. We randomly select 10 skulls of male and female and their corresponding faces from the database.

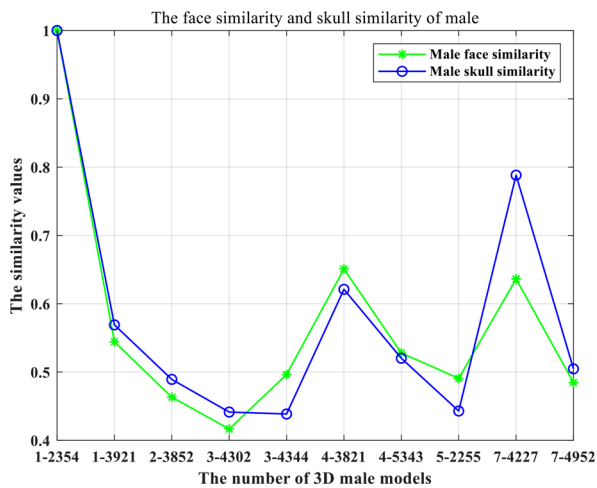


**Fig. 18** Visual thermodynamic diagram of the skull and face similarity results for males

We calculate the skull similarity and face similarity both for males and females, by comparing the male No. 001-2354 model with the other male models, respectively, and then repeating the same procedures for the female No.002-1642 model with other female models. In Fig. 16, we show the five males which are the most similar to No. 001-2354 male, including the faces and skulls. In Fig. 17, we show the five females which are the most similar to female No.002-1642, including the faces and skulls. We see that the results shown in Figs. 16 and 17 are consistent with the results we discussed above for face similarity between males and females. This consistency of results indicates the effectiveness of our proposed method.

#### 4.5 Craniofacial relationship

Figures 18 and 19 show line graphs of the similarity change trends for both males and female skulls and faces based on HWKS (male No.001-2354 to other male models; female No.002-1642 to other female models).

From Fig. 18, when the similarity between the No.001-2354 skull and other male skulls decreases, the similarity between the No.001-2354 face and other faces also decreases. Male's skull similarity and face similarity trends are exactly the same.

From Fig. 19, the skulls similarity and the faces similarity of females show basically consistent trends, when the similarity between the female No.002-1642 skull and other female skulls decreases, the similarity between the female No.002-1642 face and other female faces also always decreases. Importantly, we discover that the divergence of a male's skull and face similarity trend is closer than that of a female. Because a male's facial features are more prominent, and

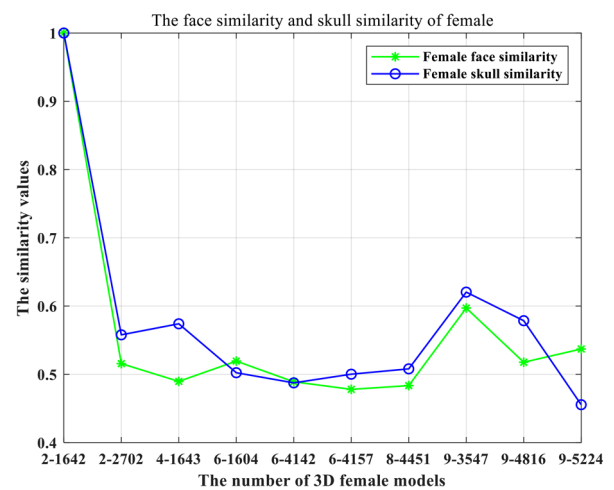


**Fig. 19** Visual thermodynamic diagram of the skull and face similarity results for females

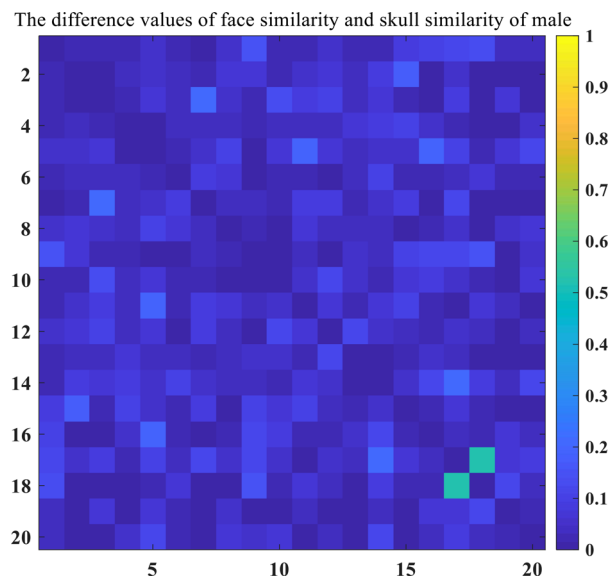


**Fig. 20** Visual thermodynamic diagram of the skull and face similarity results for males

male skull shape can better determine male face shape. The results indicates the effectiveness of our proposed method.

The above experimental results show that skull similarity and face similarity exhibit similar trends. To discuss the validity and rationality of the fact that 3D skull similarity can be presented by its corresponding or reconstructed face similarity, we provide the matrix diagrams of the similarity differences between skulls and faces of males and females, which are shown as Figs. 20 and 21. From Figs. 20 and 21, we can see that the difference between the skull similarity value and the face similarity value is smaller for both males and females, on the whole, indicating the effectiveness of using the corresponding face similarity result to present the skull similarity.

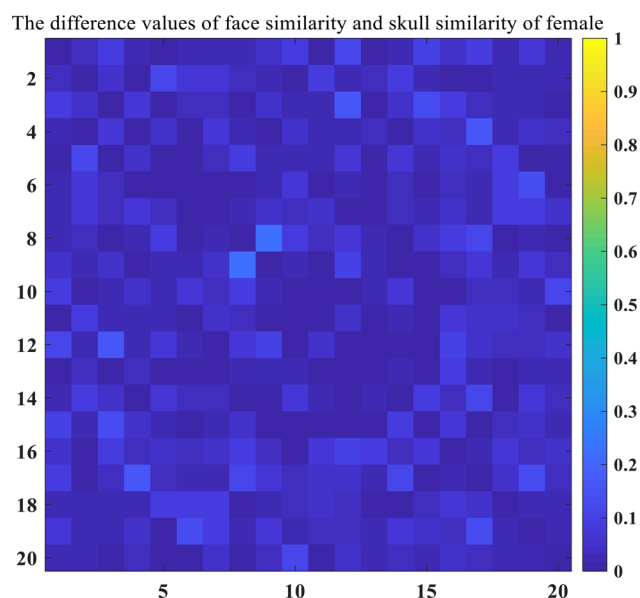


**Fig. 21** Visual thermodynamic diagram of the skull and face similarity results for females

## 5 Conclusion

In this article, we define an efficient shape descriptor, HWKS involving the LBO. The defined HWKS is convenient for extracting and representing 3D skull and facial features. Based on the HWKS, we provide a 3D skull similarity and face similarity measurement pipeline, the effectiveness and accuracy of which has been corroborated by both linear interpolation similarity experiments and real data experiments. Furthermore, since our pipeline is applicable for similarity measurement of 3D skulls without the need of filling holes and is robust for 3D facial expression transformation, users will encounter no difficulty in generalizing our framework for use according to their differentiated needs. Under our proposed unified measurement framework, we simply probed craniofacial relationship to show the effectiveness of 3D skull similarity can be presented by its corresponding or reconstructed face similarity.

**Acknowledgements** The authors like to thank the support of National Key Cooperation between the BRICS Program of China (No.2017YFE 0100500); National Key R&D Program of China (No.2017YFB1002604, No.2017YFB1402105, No.2017YFB1002804); Beijing Natural Science Foundation of China (No. 4172033).

## Compliance with ethical standards

**Conflict of interest** The authors declare that they have no conflict of interest.

## References

1. Pei, Y., Zha, H., Yuan, Z.: The craniofacial reconstruction from the local structural diversity of skulls. *Comput. Graphics Forum* **27**(7), 1711–1718 (2008)
2. Giurazza, F., Del Vescovo, R., Schena, E., Battisti, S., Cazzato, R.L., Grasso, F.R., Silvestri, S., Denaro, V., Zobel, B.B.: Determination of stature from skeletal and skull measurements by ct scan evaluation. *Forensic Sci. Int.* **222**(1–3), 398e1 (2012)
3. Spradley, M.K., Jantz, R.L.: Sex estimation in forensic anthropology: skull versus postcranial elements. *J. Forensic Sci.* **56**(2), 289–296 (2011)
4. Damas, S., Cordón, O., Ibáñez, O., Santamaría, J., Alemán, I., Botella, M., Navarro, F.: Forensic identification by computer-aided craniofacial superimposition: a survey. *ACM Comput. Surv. (CSUR)* **43**(4), 27 (2011)
5. Fenton, T.W., Heard, A.N., Sauer, N.J.: Skull-photo superimposition and border deaths: identification through exclusion and the failure to exclude. *J. Forensic Sci.* **53**(1), 34–40 (2008)
6. Shrimpton, S., Daniels, K., De Greef, S., Tilotta, F., Willems, G., Vandermeulen, D., Suetens, P., Claes, P.: A spatially-dense regression study of facial form and tissue depth: towards an interactive tool for craniofacial reconstruction. *Forensic Sci. Int.* **234**, 103–110 (2014)
7. Xia, J., Ip, H.H., Samman, N., Wang, D., Kot, C.S., Yeung, R.W., Tideman, H.: Computer-assisted three-dimensional surgical planning and simulation: 3D virtual osteotomy. *Int. J. Oral Maxillofac. Surg.* **29**(1), 11–17 (2000)
8. Zhao, L., Patel, P.K., Cohen, M.: Application of virtual surgical planning with computer assisted design and manufacturing technology to cranio-maxillofacial surgery. *Arch. Plast. Surg.* **39**(4), 309 (2012)
9. Zhang, L., Razdan, A., Farin, G., Femiani, J., Bae, M., Lockwood, C.: 3D face authentication and recognition based on bilateral symmetry analysis. *Vis. Comput.* **22**(1), 43–55 (2006)
10. Lei, Y., Bennamoun, M., Hayat, M., Guo, Y.: An efficient 3d face recognition approach using local geometrical signatures. *Pattern Recognit.* **47**(2), 509–524 (2014)
11. Emambakhsh, M., Evans, A.: Nasal patches and curves for expression-robust 3d face recognition. *IEEE transactions on pattern analysis and machine intelligence* **39**(5), 995–1007 (2016)
12. Hou, X.-N., Ding, S.-H., Ma, L.-Z., Wang, C.-J., Li, J.-L., Huang, F.-Y.: Similarity metric learning for face verification using sigmoid decision function. *Vis. Comput.* **32**(4), 479–490 (2016)
13. Soltanpour, S., Boufama, B., Wu, Q.J.: A survey of local feature methods for 3D face recognition. *Pattern Recognit.* **72**, 391–406 (2017)
14. Zhao, J.-L., Wu, Z.-K., Pan, Z.-K., Duan, F.-Q., Li, J.-H., Lv, Z.-H., Wang, K., Chen, Y.-C.: 3D face similarity measure by fréchet distances of geodesics. *J. Comput. Sci. Technol.* **33**(1), 207–222 (2018)
15. Lv, C., Wu, Z., Wang, X., Zhou, M., Toh, K.-A.: Nasal similarity measure of 3D faces based on curve shape space. *Pattern Recognit.* **88**, 458–469 (2019)
16. Jin, W.-X., Li, K., Geng, G.-H., Liu, L.-C.: Similarity measurement method of skull and craniofacial data. *Appl. Res. Comput.* **10**, 61 (2013)
17. Mendonca, D.A., Naidoo, S.D., Skolnick, G., Skladman, R., Woo, A.S.: Comparative study of cranial anthropometric measurement by traditional calipers to computed tomography and three-dimensional photogrammetry. *J. Craniofac. Surg.* **24**(4), 1106–1110 (2013)
18. Pei, Y., Kou, L., Zha, H., Anatomical structure similarity estimation by random forest. In: *IEEE International Conference on Image Processing (ICIP)*. IEEE, pp. 2941–2945 (2016)

19. Quatrehomme, G., Cotin, S., Subsol, G., Delingette, H., Garidel, Y., Grévin, G., Fidrich, M., Baillet, P., Ollier, A.: A fully three-dimensional method for facial reconstruction based on deformable models. *J. Forensic Sci.* **42**(4), 649–652 (1997)
20. Vanezis, P., Vanezis, M., McCombe, G., Niblett, T.: Facial reconstruction using 3-d computer graphics. *Forensic science international* **108**(2), 81–95 (2000)
21. Kermi, A., Laskri, M. T.: A 3D deformable model constrained by anthropometric knowledge for computerized facial reconstructions. In: 2012 11th International Conference on Information Science, Signal Processing and their Applications (ISSPA), IEEE, 2012, pp. 924–929
22. Berar, M., Tilotta, F.M., Glaunes, J.A., Rozenholc, Y.: Craniofacial reconstruction as a prediction problem using a latent root regression model. *Forensic Sci. Int.* **210**(1–3), 228–236 (2011)
23. Mansour, R.F.: Evolutionary computing enriched ridge regression model for craniofacial reconstruction. In: *Multimedia Tools and Applications*, pp. 1–18 (2017)
24. Duan, F., Yang, Y., Li, Y., Tian, Y., Lu, K., Wu, Z., Zhou, M.: Skull identification via correlation measure between skull and face shape. *IEEE Trans. Inf. Forensics Secur.* **9**(8), 1322–1332 (2014)
25. Shui, W., Zhou, M., Maddock, S., He, T., Wang, X., Deng, Q.: A pca-based method for determining craniofacial relationship and sexual dimorphism of facial shapes. *Comput. Biol. Med.* **90**, 33–49 (2017)
26. Berar, M., Desvignes, M., Bailly, G., Payan, Y.: 3D statistical facial reconstruction. In: *ISPA 2005, Proceedings of the 4th International Symposium on Image and Signal Processing and Analysis*, 2005. IEEE, pp. 365–370 (2005)
27. Suetens, P., Willems, G., Vandermeulen, D., De Greef, S., Claes, P.: Statistically deformable face models for cranio-facial reconstruction. *J. Comput. Inf. Technol.* **14**(1), 21–30 (2006)
28. Bronstein, A.M., Bronstein, M.M., Kimmel, R.: Three-dimensional face recognition. *Int. J. Comput. Vis.* **64**(1), 5–30 (2005)
29. Kakadiaris, I.A., Passalis, G., Toderici, G., Murtuza, M.N., Lu, Y., Karampatziakis, N., Theoharis, T.: Three-dimensional face recognition in the presence of facial expressions: an annotated deformable model approach. *IEEE Trans. Pattern Anal. Mach. Intell.* **29**(4), 640–649 (2007)
30. Smeets, D., Fabry, T., Hermans, J., Vandermeulen, D., Suetens, P.: Isometric deformation modeling using singular value decomposition for 3D expression-invariant face recognition. In: 2009 IEEE 3rd International Conference on Biometrics: Theory, Applications, and Systems, IEEE, pp. 1–6 (2009)
31. Hu, J., Hua, J.: Salient spectral geometric features for shape matching and retrieval. *Vis. Comput.* **25**(5-7):667–675 (2009)
32. Rustamov, R. M.: Laplace-Beltrami eigenfunctions for deformation invariant shape representation. In: *Proceedings of the fifth Eurographics Symposium on Geometry Processing*, Eurographics Association, pp. 225–233 (2007)
33. Ovsjanikov, M., Sun, J., Guibas, L.: Global intrinsic symmetries of shapes. In: *Computer Graphics Forum*, Vol. 27. Wiley, New York, pp. 1341–1348 (2008)
34. Sun, J., Ovsjanikov, M., Guibas, L.: A concise and provably informative multi-scale signature based on heat diffusion. In: *Computer Graphics Forum*, Vol. 28. Wiley, New York, pp. 1383–1392 (2009)
35. Aubry, M., Schlickewei, U., Cremers, D., The wave kernel signature: a quantum mechanical approach to shape analysis. In: *IEEE International Conference on Computer Vision Workshops (ICCV workshops)*. IEEE 2011, pp. 1626–1633 (2011)
36. Melzi, S., Ren, J., Rodolà, E., Sharma, A., Wonka, P., Ovsjanikov, M.: Zoomout: spectral upsampling for efficient shape correspondence. *ACM Trans. Graph. (TOG)* **38**(6), 155 (2019)
37. Xu, G.: Discrete Laplace–Beltrami operators and their convergence. *Comput. Aid. Geom. Des.* **21**(8), 767–784 (2004)
38. Ovsjanikov, M., Ben-Chen, M., Solomon, J., Butscher, A., Guibas, L.: Functional maps: a flexible representation of maps between shapes. *ACM Trans. Graph. (TOG)* **31**(4), 30 (2012)
39. Zhang, D., Wu, Z., Wang, X., Lv, C., Zhou, M.: Harmonic wave kernel signature for three-dimensional skull similarity measurements. In: *IEEE Conference on Cyberworlds (CW)*, pp. 77–84 (2019)

**Publisher's Note** Springer Nature remains neutral with regard to jurisdictional claims in published maps and institutional affiliations.

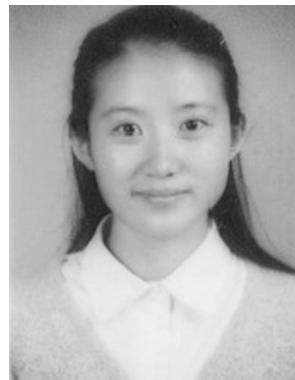


**Dan Zhang** is pursuing PhD degree in School of Artificial Intelligence, Beijing Normal University (BNU). Her research interests include computer vision, craniofacial morphology, computer graphics and discrete differential geometry.



**Zhongke Wu** is a Full Professor in School of Artificial Intelligence, Beijing Normal University (BNU), China. Currently, he is the member of Steering Committee for Professional Teaching of Animation, Digital Media in Colleges and universities of Ministry of Education, China, and member of CCF CAD and Graphics and CCF Human Computer Interaction. He led and took part in various research and development projects in computer graphics and related areas. Prof. WU's current

research interests include computer graphics, animation virtual reality, geometric modeling, volume graphics and medical imaging.



**Xingce Wang** is a Full Professor in School of Artificial Intelligence, Beijing Normal University, PR China. She has major in the 3D modeling and 3D visualization. Her current research interests include computer graphics, medical imaging, artificial intelligence and machine learning.



**Chenlei Lv** is pursuing PhD degree in School of Artificial Intelligence, Beijing Normal University (BNU). His research interests include computer vision, 3D biometrics, computer graphics, discrete differential geometry and conformal geometry.



**Na Liu** is pursuing PhD degree in School of Artificial Intelligence, Beijing Normal University (BNU). Her current research interests include computer graphics, artificial intelligence and machine learning.